

Symmetry-broken MoS₂ nanotubes through sequential sulfurization of MoO₂ nanowires

Received: 16 March 2025

Accepted: 18 August 2025

Published online: 25 September 2025



Lei Luo^{1,2,3,4,9}, Yao Wu^{4,9}, Lei Li^{1,2,3,9}, Zhonghan Zhang⁴, Lu Zheng^{1,2,3}, Chao Zhu⁴, Manzhang Xu^{1,2,3}, Weiwei Li^{1,2,3}, Ruihuan Duan⁴, Yanchao He⁴, Xin Zhou⁴, Qundong Fu^{4,5}, Gang Wu⁴, Jiefu Yang⁴, Qi Wu⁴, Wei Huang^{1,2,3,6,7}, Xuewen Wang^{1,2,3} ✉ & Zheng Liu^{4,8} ✉

Transition metal dichalcogenide (TMD) nanotubes are emerging quantum materials with distinctive symmetry-breaking properties, offering significant potential for energy conversion technologies. However, the direct synthesis of crystalline MoS₂ nanotubes remains challenging due to limited understanding of their high-temperature growth mechanisms. Here, we present a robust and controllable strategy for the direct growth of crystalline MoS₂ nanotubes with well-defined tubular morphology and high structural uniformity. This approach features two key innovations: first, the controlled introduction of hydrogen reduces MoO₃ into one-dimensional (1D) tetragonal MoO₂ (space group I4/m) chains via a vapor–liquid–solid (VLS) mechanism; second, precise temperature zoning ensures timely sulfur vapor infusion for complete sulfurization. The intermediate MoO₂ phase, with its singular crystallographic orientation, acts as an ideal template for nanotube formation. Tellurium (Te) serves as a fluxing mediator to promote the formation of uniform MoO₂ nanowires, which are subsequently converted into MoS₂ nanotubes. By systematically tuning the hydrogen concentration, we reveal its critical role in directing product morphology. The resulting MoS₂ nanotubes exhibit pronounced symmetry breaking and significant bulk photovoltaic performance, achieving a photoresponsivity of 510 A cm⁻² under 1.88 × 10⁴ W cm⁻² illumination. This work advances both the fundamental understanding of nanotube growth and the development of symmetry-engineered optoelectronic materials.

One-dimensional (1D) nanotubes derived from van der Waals (vdW) layered quantum materials have attracted considerable attention in nanomaterial research, owing to their distinct physical and chemical properties compared to their two-dimensional (2D) counterparts^{1–8}.

Transition metal dichalcogenide (TMD) nanotubes, as an emerging class of vdW nanotubes, possess non-centrosymmetric lattices and inherent lattice strain, resulting in highly polarized structures characterized by broken inversion symmetry⁹. These structures exhibit

¹State Key Laboratory of Flexible Electronics (LoFE) & Institute of Flexible Electronics (IFE), Northwestern Polytechnical University, Xi'an, China. ²Shaanxi Key Laboratory of Flexible Electronics, Northwestern Polytechnical University, Xi'an, China. ³MIIT Key Laboratory of Flexible Electronics (KLoFE), Northwestern Polytechnical University, Xi'an, China. ⁴School of Materials Science and Engineering, Nanyang Technological University, Singapore, Singapore. ⁵Beijing Institute of Technology, Zhuhai, China. ⁶State Key Laboratory of Flexible Electronics (LoFE) & Institute of Advanced Materials (IAM), Nanjing University of Posts & Telecommunications, Nanjing, China. ⁷Key Laboratory of Flexible Electronics (KLoFE) and Institute of Advanced Materials (IAM), Nanjing Tech University, Nanjing, China. ⁸CINTRA CNRS/NTU/THALES, UMI 3288, Research Techno Plaza, Singapore, Singapore. ⁹These authors contributed equally: Lei Luo, Yao Wu, Lei Li. ✉e-mail: iamxwwang@nwpu.edu.cn; z.liu@ntu.edu.sg

intriguing electrical and optical properties, thereby offering broad application prospects in fields such as superconductivity¹⁰, intrinsic photovoltaic effects¹¹, and catalysis¹². In comparison to carbon nanotubes, TMD nanotubes possess potentially more intriguing physical and chemical properties due to their richer elemental composition and tunable bandgap. However, research in this area remains limited, likely due to the challenges associated with their synthesis. In contrast to the facile synthesis of planar TMDs, transforming their layered chalcogen-metal-chalcogen structures into tubular forms requires overcoming more elastic energy, and the structural stability of few-layer products needs to be considered¹³. Owing to the influence of weak vdW forces between layers, vdW layered materials are more prone to forming hollow nanostructures (such as nanotubes or nanoscrolls) rather than tightly bonded solid nanowires when synthesized into 1D structures through chemical reactions. Tubular TMD nanostructures are typically synthesized via a solid-gas method under high-temperature conditions. Similar to the synthesis of carbon nanotubes, using metallic nanoparticles as catalysts is an effective approach for producing TMD nanotubes^{14,15}. However, a significant drawback of the catalyzed chemical vapor deposition (CVD) process is the presence of residual metallic nanoparticle impurities embedded within the nanotubes, which degrade their electronic properties by limiting electron mobility. As an alternative, sulfurization of precursors leveraging the Kirkendall effect has also proven to be an effective method for forming tubular TMD structures¹⁶. Although significant progress has been made in developing template-based tubular materials using nanowhisker precursors¹⁷, challenges remain due to the complexities and stability issues associated with precursor selection.

Recent studies have reported the synthesis of tubular TMD materials using metal suboxides, particularly tungsten suboxides^{18,19}. However, due to factors such as stability, suitable molybdenum suboxides for use as precursors are relatively scarce. Herein, we report an efficient strategy for the direct synthesis of 1D MoS₂ nanotubes with high crystallinity and rhombohedral (3R) interlayer stacking. The method involves the introduction of hydrogen gas during a controlled CVD process. Typically, sulfurization of precursors using the Kirkendall effect requires the precursor to be prepared as 1D whisker-like nanomaterials in advance²⁰. We controlled the participation time of the volatile source in the reaction by placing it in different temperature zones. First, MoO₃ was reduced to tetragonal MoO₂ (I4/m group) under the fluxing action of Te and the reducing action of hydrogen gas, forming 1D nanowires through a VLS growth mode. Subsequently, sulfur vapor participated in the reaction to sulfurize the MoO₂ nanowires, eventually forming few-layer MoS₂ nanotubes with a high aspect ratio. We conducted a detailed study of the entire reaction process and growth mechanism. Compared to 2D MoS₂, the 1D tubular MoS₂ exhibits strong symmetry-breaking effects, leading to promising performance in the bulk photovoltaic effect (BPVE), which has the potential to study non-centrosymmetric quantum phenomena in fundamental physics^{21,22}.

Results

Direct growth and morphology control of MoS₂ nanotubes

The hydrogen-assisted synthesis of MoS₂ nanotubes is schematically illustrated in Fig. 1a. The growth temperature setting has been divided into four stages (Fig. 1b). As shown in Fig. 1c, in the heating stage, the MoO₃ powder begins to melt and volatilize under the fluxing action of Te powder^{23,24}, and nucleates as a Mo–O–Te liquid phase on the SiO₂/Si substrate. As the saturated vapor pressure of MoO₃ increases, MoO₂ nanowires begin to precipitate from the liquid nucleation points under the reducing action of hydrogen gas. This process is a typical VLS growth model²⁵. Furthermore, as the temperature increases, the concentration of sulfur vapor begins to rise, reacting with hydrogen to form H₂S. The sulfidation of MoO₂ nanowires is initiated, eventually resulting in the formation of hollow MoS₂ nanotubes via the Kirkendall

effect¹⁶. The schematic diagram of the modified CVD equipment for growing MoS₂ nanotubes is shown in Supplementary Fig. 1. All reactants are placed in a smaller quartz tube with one end sealed, arranged according to different temperature zones. Our simulation results indicate that the internal quartz ampule plays a crucial role in decreasing the rate of gas flow (Supplementary Fig. 2)²⁶. This reduction ensures that atoms are deposited and undergo reactions mainly through diffusion, thereby maintaining an adequate concentration of reactants. MoO₃ powder is placed in the highest temperature zone of the tube furnace, facilitating the volatilization reaction. In our synthesis process, Te plays a pivotal but non-structural role as a fluxing promoter. The introduction of Te significantly reduces the melting point of MoO₃ by forming a low-melting eutectic phase or volatile Mo–Te intermediates. This assists the formation of 1D tetragonal MoO₂ nanowires via a VLS mechanism under hydrogen reduction. Without Te, MoO₃ tends to sublime unevenly and fails to produce uniform nanowire structures, as confirmed by our control experiments (Supplementary Table 1). During the sulfurization stage, Te has already evaporated or been carried away by carrier gas, and our XPS and EDX analyses (Supplementary Fig. 3) confirm the absence of Te in the final MoS₂ nanotubes. Therefore, Te acts exclusively as a reaction mediator and fluxing agent, not as a dopant or structural constituent. This behavior is distinct from systems like MoTe₂, where Te is a necessary chalcogen source and integrates into the final lattice^{27,28}. Here, Te enables the initial MoO₂ nanowire formation, which is essential for the subsequent symmetry-directed transformation into hollow MoS₂ nanotubes via the Kirkendall effect^{23,29}. In our method, the MoS₂ nanotubes can be well synthesized under a reaction temperature range of 750 to 800 °C, with an optimal temperature of 770 °C (Supplementary Fig. 4). The other details of the growth conditions are shown in the “Methods” section.

Furthermore, our studies have revealed that the morphology of the products can be regulated by controlling the concentration of H₂ during the reaction process. As illustrated in Fig. 1d, in the absence of H₂, under the thermodynamic growth mode, the MoO₃ source ultimately undergoes epitaxial growth with sulfur to form 2D MoS₂³⁰ (Fig. 1e). When a small amount of H₂ (5%) is involved in the reaction process, the final product is a composite structure of 2D MoS₂ film and MoS₂ nanotubes (Fig. 1f). As the concentration of H₂ further increases (15%), the underlying MoS₂ film of the product begins to contract and forms 2D ribbon-like materials along the MoS₂ nanotubes (Fig. 1g). When the proportion of hydrogen gas reaches 30% in the argon–hydrogen gas mixture, the final product is pure MoS₂ nanotube (Fig. 1h). Interestingly, as shown in Supplementary Figs. 5 and 6, when we changed the growth substrate from SiO₂/Si to f-mica, we found that the samples transformed from curved nanotubes to straight nanotubes, which were arranged at 0°, 60°, and 120° on the substrate. Meanwhile, we examined the curvature behavior of nanotubes with different lengths (Supplementary Fig. 7), the transformation clearly demonstrates the strong influence of substrate choice and nanotube length on their morphology and orientation: while longer nanotubes tend to bend on rigid substrates like SiO₂/Si due to accumulated internal strain, they remain straight and well-aligned on atomically flat, lattice-matched substrates such as f-mica. This indicates that the substrate can effectively regulate the alignment of the product³¹.

Characterization of MoO₂ nanowires in the sulfidation process

In our experimental design, we isolated tetragonal-phase MoO₂, a key intermediate in the formation of MoS₂ nanotubes. As shown in Supplementary Table 1, the sulfur source was removed during CVD synthesis. Optical and scanning electron microscope (SEM) images of the resulting products (Fig. 2a, b) reveal 1D nanomaterials with high aspect ratios, whose ends are decorated with nanoparticles. The growth of MoO₂ nanowires follows a hydrogen- and Te-assisted VLS mechanism^{32,33}. Under a reducing atmosphere, Te lowers the melting

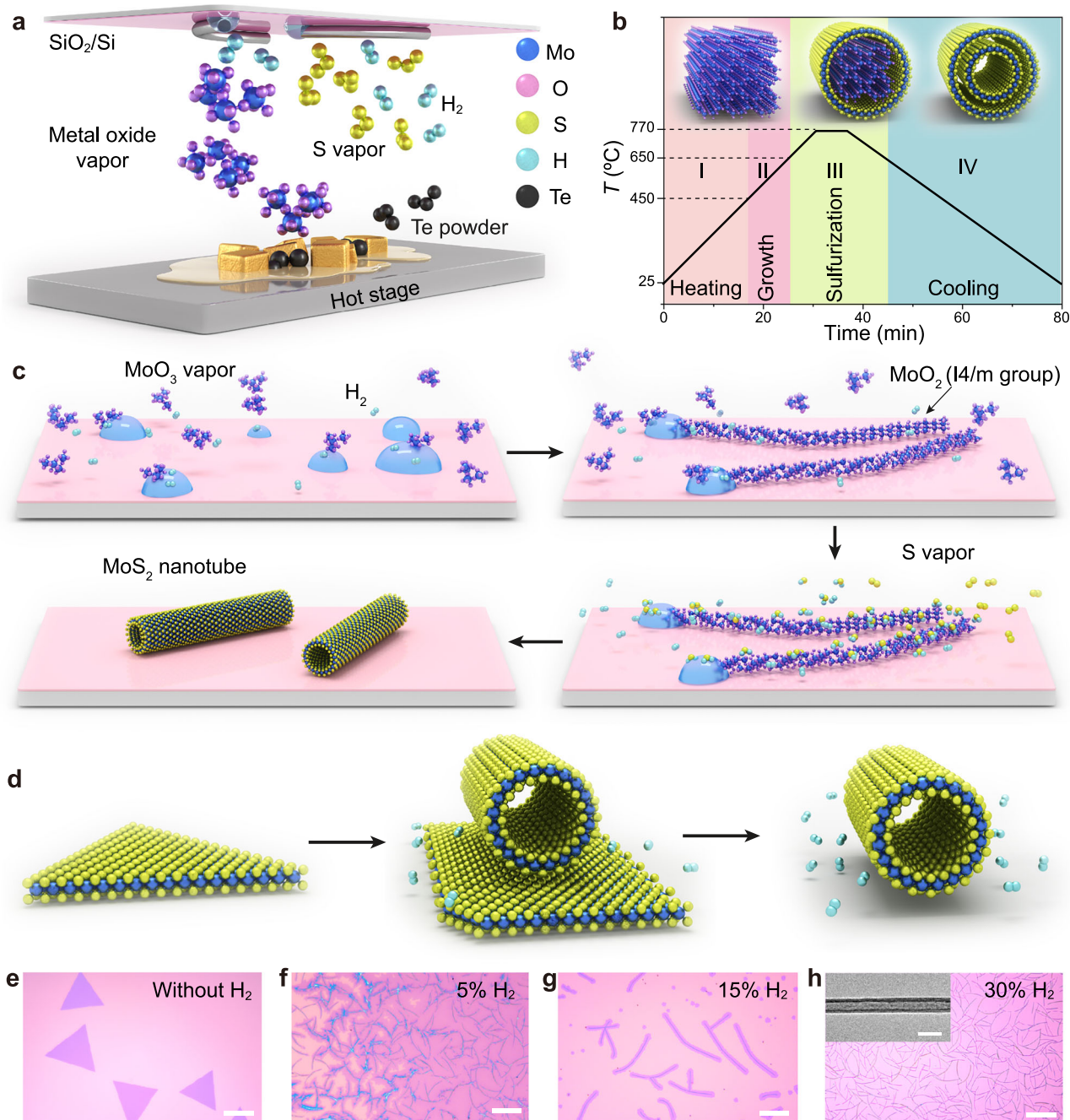


Fig. 1 | Hydrogen-assisted synthesis of MoS₂ nanotubes and the control of product morphology. **a** Schematic of the synthesis of MoS₂ nanotubes by CVD. **b** Temperature profile for synthesizing MoS₂ nanotubes, including Stage I: heating; Stage II: growth; Stage III: sulfurization; and Stage IV: cooling. Corresponding schematic diagrams of the products (MoO₂ nanowires, MoS₂-MoO₂ core-shell structures, and MoS₂ nanotubes, respectively) at different stages. **c** Proposed growth mechanism of MoS₂ nanotubes. The process begins with nucleation and

formation of tetragonal MoO₂ via a VLS growth mechanism, which is subsequently transformed into MoS₂ nanotubes through sulfidation. **d** Schematic illustration of the morphological changes of products under different H₂ concentrations.

e-h Optical microscopy images showing the morphology evolution from 2D MoS₂ flakes to MoS₂ nanotubes with increasing H₂ concentration from 0% to 30%, the inset in **(h)** shows a TEM image of a single MoS₂ nanotube. Scale bar: 40 μm in **(e-h)**, and 50 nm in the inset of **(h)**. Source data are provided as a Source Data file.

point of MoO₃ and facilitates the formation of a liquid droplet that mediates axial nanowire elongation. As the local MoO₃ vapor pressure increases, molybdenum species dissolve into the liquid droplet until supersaturation is reached. Upon supersaturation, MoO₂ begins to precipitate from the droplet, and 1D nanowires emerge as the droplet rolls forward along the substrate. After growth terminates, the droplet solidifies as a residual nanoparticle at the nanowire tip. This behavior is consistent with a typical VLS process. SEM-EDX analysis of MoO₂ nanowires with terminal nanoparticles (Supplementary Fig. 8)

confirms that Te plays a catalytic yet non-reactive role during nanowire formation. High-angle annular dark-field scanning transmission electron microscopy (HAADF-STEM) image and energy-dispersive X-ray spectroscopy (EDS) mappings (Fig. 2c) confirm that the 1D structures are solid, uniform nanowires with evenly distributed molybdenum and oxygen elements. The atomic structure in the (001) and (100) directions is shown in Fig. 2d, e. These clearly demonstrate that the material is a tetragonal phase of MoO₂ with the space group I4/m. Cross-sectional atomic-resolution STEM imaging of a MoO₂ nanowire (Fig. 2f)

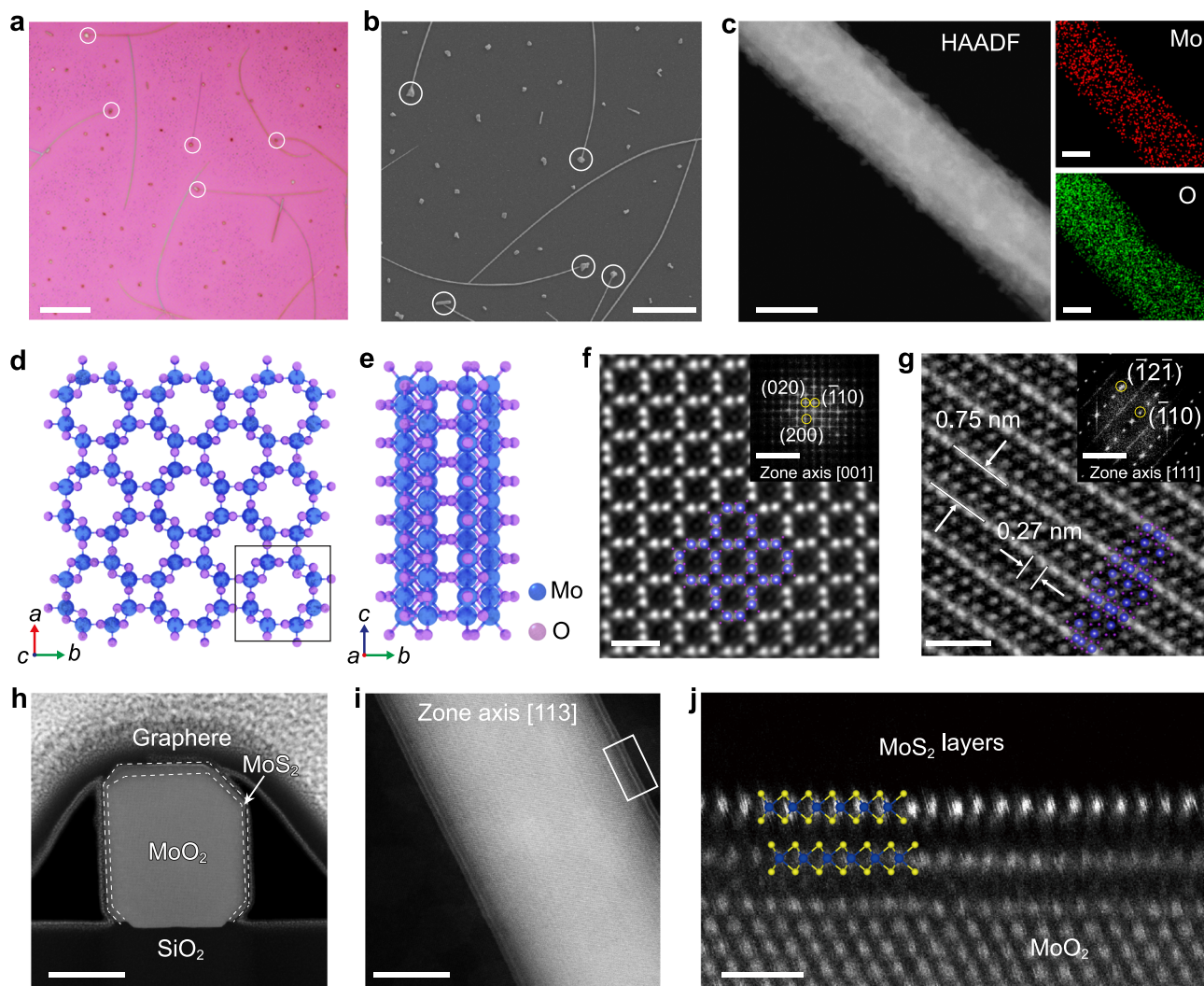


Fig. 2 | Microscopy analysis of MoO₂ nanowires. **a, b** Optical and SEM images showing MoO₂ nanowires grown on SiO₂/Si substrate. Terminal particles attached to the nanowires are highlighted with circles. **c** HAADF-STEM image and corresponding EDS elemental mappings of a single MoO₂ nanowire. **d, e** Atomic structure of tetragonal MoO₂ (viewed from *c*-axis and *a*-axis). **f** Cross-sectional STEM image of Tetragonal MoO₂ nanowires. The inset in (f) displays the corresponding fast Fourier transform pattern. **g** STEM image of tetragonal MoO₂ from the (111)

direction. The inset shows the corresponding FFT pattern. **h** Cross-sectional STEM image of the initial stage of the sulfidation process of MoO₂ nanowires. **i, j** HAADF-STEM image of the initial stage of the sulfidation process from zone axis [113]. And a magnified view of the region denoted by a white dashed square shows the synthesized MoS₂ stacked in a rhombohedral stacking manner. Scale bar: 10 μm in (a), 5 μm in (b), 50 nm in (c), 1 nm in (f, g), 5 nm⁻¹ in insets of (f, g), 20 nm in (h), 10 nm in (i), 1 nm in (j).

reveals a high degree of symmetry, consistent with a tetragonal-phase single crystal viewed along the (001) direction. Figure 2g is an atomic-resolution STEM image along the (111) direction, revealing two distinct sets of lattice fringes with average spacings of 0.75 nm, corresponding to the ($\bar{1}10$) and ($\bar{1}2\bar{1}$) planes of the tetragonal phase MoO₂. Furthermore, Raman spectroscopy was performed on MoO₂ nanowires (Supplementary Fig. 9), and DFT calculations were conducted to analyze their vibrational modes in the idealized bulk state. Comparison between theory and experiment revealed three matching vibrational peaks at 152 cm⁻¹, 185 cm⁻¹, and 295 cm⁻¹. The remaining discrepancies are likely due to the rod-like morphology of the sample, which deviates from the ideal bulk crystal and alters its vibrational response under laser excitation.

The Kirkendall effect enables a solid cylindrical structure to transform into a hollow morphology via diffusion and lattice rearrangement^{16,19}. As the temperature in the sulfur-source zone increases, the corresponding rise in sulfur vapor pressure initiates its participation in the reaction. Assisted by H₂, the MoO₂ nanowires

undergo sulfidation. This transformative phase culminates in the formation of MoS₂ nanotubes. By controlling the reaction time, we obtained samples in the initial stage of sulfidation (1 min). Figure 2h presents a representative cross-section STEM image of MoO₂ nanowire in the initial stage of sulfidation, showing a MoS₂ shell enveloping the MoO₂ core. Observations along the (113) crystallographic direction (Fig. 2i, j) show that the MoS₂ layers on the MoO₂ surface exhibit 3R stacking.

Taken together, we propose that the formation of MoS₂ nanotubes in our system likely proceeds via a hybrid mechanism, summarized as follows: Following the growth of 1D tetragonal-phase MoO₂ nanowires through a VLS mechanism, the introduction of sulfur vapor at elevated concentrations, combined with the presence of hydrogen, initiates the sulfidation process. In the early stages, the outer shell of the MoO₂ nanowire undergoes sulfidation first. This transformation induces lattice distortions and local defect formation, which in turn trigger the onset of the hollowing process. These structural defects, particularly near the tube tip (Supplementary Fig. 10), facilitate the

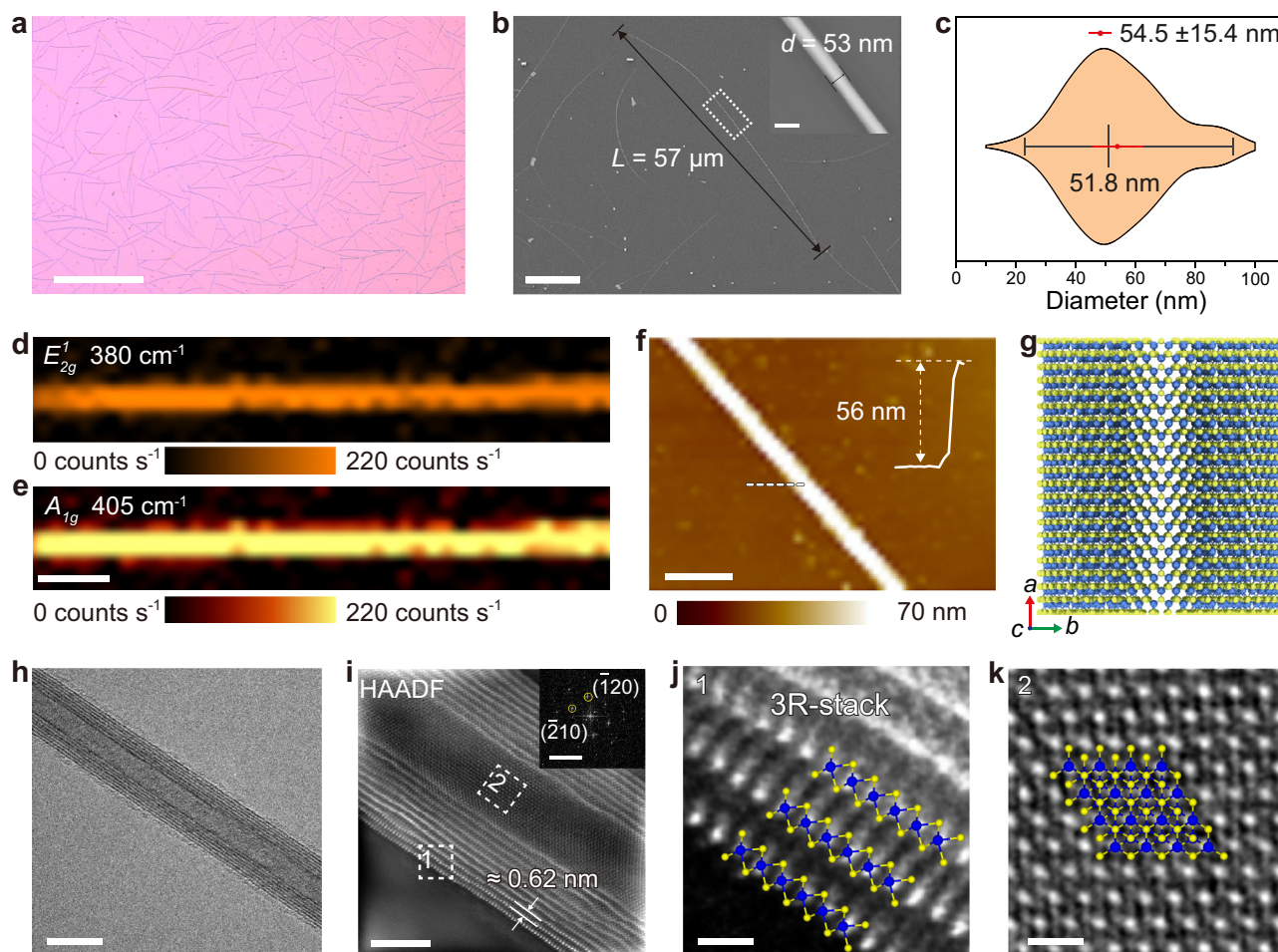


Fig. 3 | Characterization of MoS₂ nanotubes. **a** Bright optical image of MoS₂ nanotubes grown on SiO₂/Si substrate. **b** SEM image shows that the MoS₂ nanotubes have a large aspect ratio. **c** Violin plot of nanotube diameters ($n = 80$), with mean (54.5 ± 15.4 nm) and median (51.8 nm) indicated. **d, e** Raman intensity mapping for E_{2g}^1 (380 cm^{-1}) and A_{1g} (405 cm^{-1}), respectively. **f** AFM image illustrating that pure MoS₂ nanotubes can be obtained under appropriate H₂ concentration ratios. **g** Structural characterization of multiwall MoS₂ nanotubes. **h** Bright field TEM image of completely sulfurized MoS₂ nanotube. **i** HAADF-STEM image of

multiwall MoS₂ nanotube. Inset: fast Fourier transform pattern in the central region of the nanotube. **j, k** Atomic resolution HAADF-STEM image of the area denoted by white dashed squares 1 and 2 in panel **e**, revealing the characteristic arrangement of the rhombohedral symmetry (3R) phase, this pattern is superimposed and aligned with the atomic structure model for detailed comparison. Scale bar: 40 μm in (**a**), 10 μm in (**b**), and 100 nm in the inset of (**b**), 1 μm in (**d, e**), 100 nm in (**f**), 20 nm in (**h**), 5 nm in (**i**), and 1 nm⁻¹ in the inset of (**i**), 0.5 nm in (**j, k**). Source data are provided as a Source Data file.

inward diffusion of reactive gases (S/H₂), enabling continued sulfidation of the inner MoO₂ core. Concurrently, the presence of these tip defects also allows for partial Mo loss through evaporation. In addition, volatilized MoO₂ can migrate into the nanotube cavity, where it re-deposits onto the inner surface and reacts with sulfur to form additional MoS₂ layers, contributing to inner wall growth. As the internal MoO₂ core becomes fully consumed, this process results in the formation of multi-walled, hollow MoS₂ nanotubes.

Characterizations of MoS₂ nanotubes

We characterized the fully sulfurized MoS₂ nanotubes, the nanotubes synthesized on SiO₂/Si substrate exhibit an average density of ≈ 51 nanotubes per $10^4\text{ }\mu\text{m}^2$ (Supplementary Fig. 11). As shown in the characterization diagrams (Fig. 3a–c) of the MoS₂ nanotubes, the structures exhibit a high aspect ratio exceeding 1000 and an average diameter of ≈ 51 nm. STEM analysis of 50 samples indicates that the inner diameters are centered around 37 nm, with an average wall number of ≈ 13 layers (Supplementary Fig. 12). While precise control over the geometric structure is still limited, we are exploring sulfurization of pre-selected MoO₂ nanowires to improve uniformity, which shows promise for future optimization. HAADF-STEM and EDX

mapping of fully sulfurized MoS₂ nanotubes (Supplementary Fig. 13) show Mo and S signals, although accurate quantification is limited by Mo-L and S-K peak overlap. Oxygen is confined to the terminal nanoparticle, likely due to incomplete sulfurization caused by their larger size. Trace Te (0.37%) is detected, indicating minimal incorporation. These results confirm the transformation of MoO₂ into MoS₂ nanotubes. Raman intensity mapping of E_{2g}^1 (380 cm^{-1}) and A_{1g} (405 cm^{-1}) with a mapping size of $2\text{ }\mu\text{m} \times 8\text{ }\mu\text{m}$ area (Fig. 3d, e) indicates high spatial uniformity of the MoS₂ nanotubes. To probe the presence of sulfur vacancies and curvature-induced effects in the MoS₂ nanotubes, we also performed resonance Raman spectroscopy using a 633 nm excitation wavelength and compared the results with monolayer MoS₂ (Supplementary Fig. 14). The results suggest that while the nanotube geometry modifies phonon selection rules through structural anisotropy and strain, the intrinsic defect density remains low. Atomic force microscopy (AFM) testing indicated that the sample diameter is around 50 nm (Fig. 3f). Figure 3g shows a schematic diagram of a multilayer MoS₂ nanotube. The TEM image (Fig. 3h) shows that the MoS₂ nanotubes are uniform and multi-walled, a feature attributed to the high-temperature synthesis method employed. The HAADF-STEM image (Fig. 3i) reveals that the MoS₂ nanotube exhibits

high crystallinity. We conducted a magnified analysis of the atomic structure in the wall region (the white dashed box marked as 1 in Fig. 3i) and the axial central region (the white dashed box marked as 2 in Fig. 3i). Figure 3j displays the arrangement of atomic columns in S–Mo–S chevrons located at the edge of a MoS₂ nanotube. This arrangement corresponds to the 3R phase of MoS₂³⁴, as demonstrated by its alignment with the overlaid atomic structure model. The atomic arrangement in the middle of the nanotube (Fig. 3k) presents a periodic honeycomb structure along the axial direction of the nanotube, as overlaid and aligned with the atomic structure model. Additionally, a typical 3R-phase stacking pattern is observed on the tube wall (Supplementary Fig. 15). We conducted FFT analysis of atomic-resolution STEM images along [001] and [010] directions (Supplementary Fig. 16). The resulting patterns match well with simulated 3R-MoS₂ diffraction, showing strong (003) reflections and absence of 2H spots, confirming the 3R stacking order, consistent with ref. 35. These results indicate that MoO₂ nanowires will form 3R phase MoS₂ nanotubes after sulfidation in a hydrogen-assisted environment.

Optical properties and BPVE

The optical response of low-dimensional materials often reflects their structural characteristics. We compared the Raman spectra, photoluminescence (PL) signals, and polarization-dependent second harmonic signals (SHG) of 2D monolayer MoS₂ and MoS₂ nanotubes. As shown in Fig. 4a, the E_{2g}^1 vibrational mode of tubular MoS₂ exhibits a significant red shift from 384.5 cm⁻¹ in monolayer MoS₂ to 375.8 cm⁻¹ in the largest diameter nanotube, indicating a total shift of ≈ 8.7 cm⁻¹. This redshift, plotted against nanotube diameter in Fig. 4b, increases with curvature and wall number, and is attributed to in-plane tensile strain induced by the tubular geometry. In the rolled-up structure, tensile stress dominates due to the larger volume of outer layers, leading to Mo–S bond elongation and softening of the in-plane phonon mode^{36,37}. This further implies the existence of intrinsic in-plane polarization in MoS₂ nanotubes. PL test results (Supplementary Fig. 17) indicate that the PL signal is strictly distributed along the axial direction of the nanotubes, with no significant PL signals observed in the surrounding areas. This confirms that the PL originates from the nanotubes themselves. The PL spectrum shows a peak at 687 nm, corresponding to the A exciton transition. Compared with the PL peak of monolayer MoS₂ (≈ 670 nm), a significant redshift is observed. Under the same testing conditions, the PL intensity of the nanotubes is significantly lower compared to that of monolayer MoS₂³⁴. We used DFT to calculate the change in the bandgap of MoS₂ nanotubes with varying curvature and number of layers (Supplementary Fig. 18). The results show that with the increase in the curvature of the nanotubes and the number of layers, the valence band top and the conduction band bottom gradually converge³⁸. We also verified this in the transfer characteristic tests of the MoS₂ nanotube field effect transistor (Supplementary Fig. 19), and the result is consistent with the electrical properties of similarly structured TMD materials reported in refs. 34,39. Nonlinear optics can effectively analyze the symmetry of materials. The polarization-dependent SHG signal of 2D monolayer MoS₂ exhibits a classic six-fold symmetry pattern⁴⁰ (Supplementary Fig. 20), while the polarization-dependent SHG signal (Fig. 4c) of 1D tubular MoS₂ shows an anisotropic nonlinear optical response⁴¹. These significant differences in optical responses indicate a greater symmetry breaking in the MoS₂ nanotube compared to planar MoS₂.

As shown in Fig. 4d, first-principles DFT calculations on MoS₂ nanotubes show that curvature-induced lattice distortion is the dominant source of spontaneous polarization ($\Delta P_c \approx 11.5$ eÅ/Mo₄₈S₉₆), which is derived by comparing the polarization of a larger single-walled Mo₄₈S₉₆ nanotube with that of two smaller single-walled Mo₂₄S₄₈ nanotubes. Although the total atomic content is equivalent, the decrease in curvature in the larger tube leads to a net reduction in polarization, revealing the substantial role of geometric curvature in

breaking inversion symmetry. In contrast, adding extra walls contributes only a minor incremental term ($\Delta P_w \approx 0.04$ eÅ/Mo₇₂S₁₄₄). This is obtained by subtracting the combined polarization of a Mo₄₈S₉₆ tube and a Mo₂₄S₄₈ tube (representing the inner and outer walls) from that of the double-walled Mo₇₂S₁₄₄ structure. This small difference indicates that wall-number-induced polarization enhancement is significantly suppressed due to interlayer screening and saturation effects.

The BPVE of tubular TMD materials has so far only been reported in WS₂ nanotubes¹¹. To investigate the BPVE of tubular MoS₂ materials, we fabricated devices based on MoS₂ nanotubes. Firstly, we prepared a device based on a 5-layer 3R-phase MoS₂ film (Supplementary Fig. 21) and tested its response to laser illumination (Fig. 4e). The result shows that the MoS₂ flake only exhibits a photoconductive effect with a negligible short-circuit (I_{sc}) under illumination. Figure 4f presents the current-voltage (I – V) characteristics as a function of varying laser power levels (P_{laser}), illustrating that both the I_{sc} and the open-circuit voltage (V_{oc}) exhibit a monotonic variation in response to P_{laser} . The BPVE in MoS₂ nanotubes demonstrates considerable stability, both qualitatively and quantitatively. Figure 4g illustrates a simple MoS₂ nanotube photovoltaic device along with the schematic diagram of the test. Besides, we measured the I_{sc} as the laser (532 nm) spot was scanned from one electrode to another. Figure 4h indicates that the I_{sc} of the MoS₂ nanotube device is strongest when the laser is irradiated at the middle of the nanotubes. This demonstrates the BPVE of MoS₂ nanotubes, rather than the traditional Schottky-junction photovoltaic effect. As depicted in Fig. 4i, the I_{sc} undergoes alterations across numerous laser on-off cycles. Under 1.88×10^4 W cm⁻² of illumination, the photocurrent can reach 510 A cm⁻² (the diameter of the nanotube is 50 nm). I_{sc} consistently reverts to a comparable value upon the reactivation of laser illumination. Power-dependent photocurrent was measured to further clarify the physical mechanism of the BPVE observed in MoS₂ nanotubes. As shown in Fig. 4j, the photocurrent in nanotubes exhibits a transition from a linear to a square-root dependence on power as the power increases, aligning with the predictions of the theoretical shift current model and corroborating previous experimental findings. In the BPVE tests of other devices (Supplementary Fig. 22), the I_{sc} increases with the diameter of the nanotubes (indicating an increase in total polarization), as larger nanotubes inevitably possess more concentric walls. The cumulative dipolar fields from these walls, together with reduced quantum-confinement resistance, enhance carrier separation and transport, thereby outweighing the loss of curvature. Hence, curvature governs the intrinsic lattice polarization, whereas wall number and inter-wall coupling determine how that polarization translates into efficient bulk photovoltaic shift currents in practical MoS₂ nanotube devices⁴². These results indicate that MoS₂ nanotube structures have potential value for fundamental physical research.

Discussion

In this study, we have developed an efficient hydrogen-assisted CVD method for the direct synthesis of MoS₂ nanotubes with controlled crystallinity and structural uniformity. By leveraging the VLS growth process and carefully controlling the hydrogen concentration, we achieved significant control over the morphology of the final products, ranging from 2D MoS₂ films to pure MoS₂ nanotubes. The transformation from MoO₂ to MoS₂ nanotubes was driven by the Kirkendall effect, and the resulting nanotubes exhibited a high aspect ratio and 3R stacking. Our detailed structural and optical characterizations revealed the distinct properties of MoS₂ nanotubes, including strong polarization, strain-induced redshifts in Raman and PL spectra, and symmetry breaking compared to planar 2D MoS₂. Furthermore, we demonstrated the BPVE in MoS₂ nanotubes, providing a platform for investigating symmetry-breaking phenomena in fundamental physics. These findings offer insights

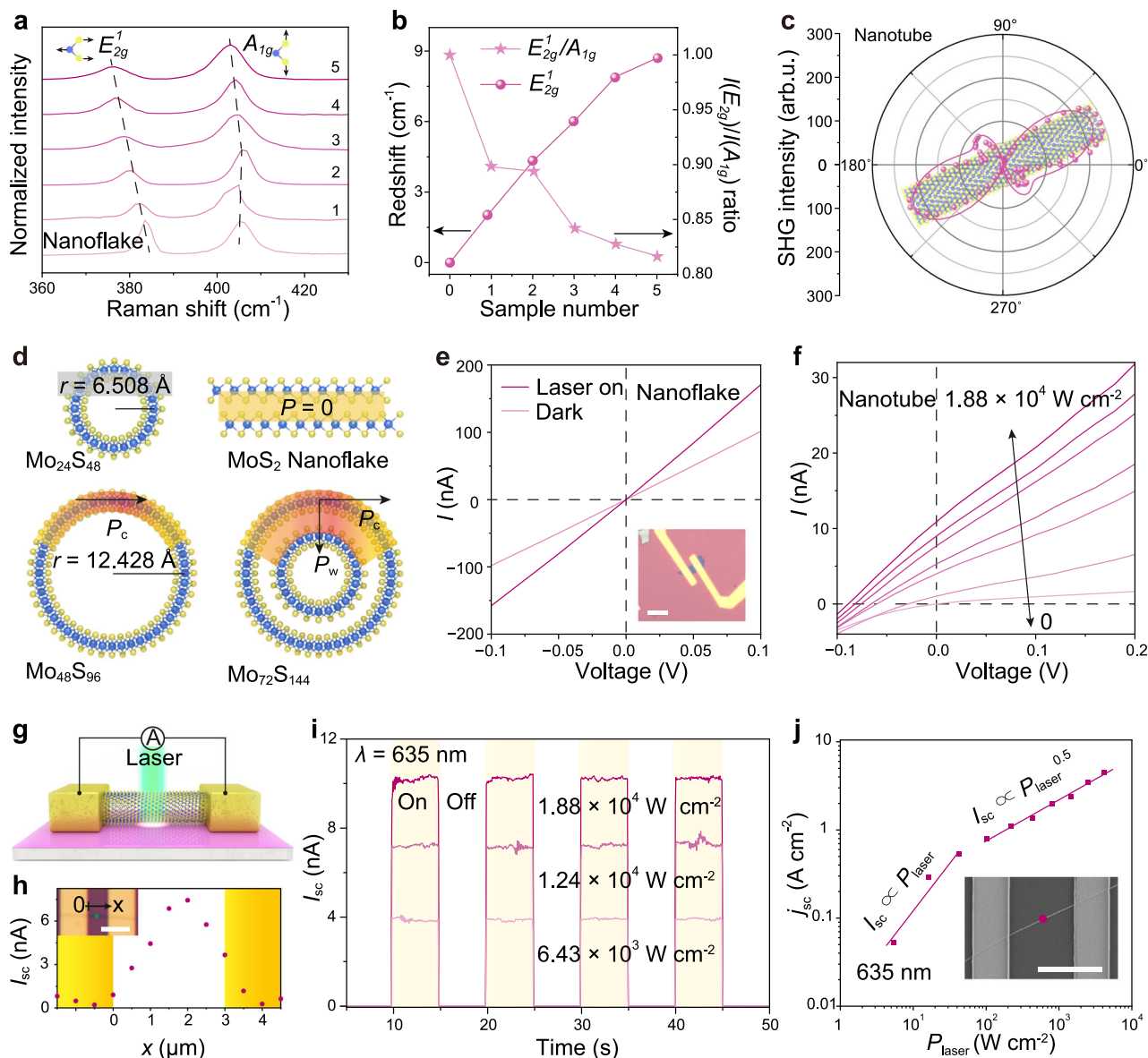


Fig. 4 | Optical properties and bulk photovoltaic response of MoS₂ nanotubes.

a Raman spectrum of MoS₂ nanotubes and monolayer MoS₂ flake, showing a curvature-induced redshift of the E_{2g}^1 mode. **b** Evolution of E_{2g}^1 peak position and E_{2g}^1/A_{1g} intensity ratio across multiple samples, indicating an increase in in-plane strain and the number of walls. **c** Polarization-dependent SHG signals of MoS₂ nanotubes. **d** DFT-calculated polarization distributions in MoS₂ nanotubes with varying curvature and wall numbers. $\Delta P_c = 11.47 \text{ eÅ}/\text{Mo}_{48}\text{S}_{96}$ —representing the polarization enhancement from curvature; $\Delta P_w = 0.04344 \text{ eÅ}/\text{Mo}_{72}\text{S}_{144}$ —the additional contribution from increased wall number. **e** I - V characteristics of few-layer 3R MoS₂ nanofilm, showing typical photoconductive behavior. **f** I - V characteristics

are recorded at different illumination intensities. The laser wavelength is 635 nm. **g** Schematic diagram of MoS₂ nanotube BPVE device. **h** The dependence of I_{sc} on the position of the laser spot in a MoS₂ nanotube device. The main response occurs when the laser spot illuminates the center of the device away from the contacts. **i** I_{sc} was measured during on/off cycles of a 635 nm laser, with three different power levels. The duration of one cycle is 10 s. **j** Incident power density dependence of j_{sc} for a BPVE device with a crossover from a linear to a square root relationship. Scale bar: 10 μm in the inset of (**e**), 5 μm in the inset of (**h**, **j**). Source data are provided as a Source Data file.

into the growth mechanisms of TMD nanotubes and indicate their relevance for advanced energy and optoelectronic technologies. Future research should focus on optimizing the synthesis process and exploring additional functionalities of MoS₂ nanotubes in practical device architectures.

Methods

Growth of MoS₂ nanotubes

The MoS₂ nanotubes were synthesized by atmospheric pressure chemical vapor deposition (APCVD). A sufficient amount of sublimed sulfur powder (Aladdin, 99.95%) was placed at the sealed end of an inner quartz tube with a diameter of 12 mm and a length of 320 mm. At

60 mm from the sulfur source, 0.05 mg of Te powder was placed in a quartz boat. A piece of SiO₂/Si substrate with a 285 nm oxidation layer is placed over a quartz boat measuring 20 mm in length, 8 mm in width, and 4 mm in height, which contains 0.2 mg of MoO₃ powder (Aladdin, 99.999%). The inner quartz tube was placed into a 2-inch quartz tube. Prior to heating, the system was purged with argon gas for 5 min. Argon and hydrogen gases were introduced as carrier and reducing gases at flow rates of 70 cm³ STP min⁻¹ and 30 cm³ STP min⁻¹, respectively. The quartz tubes were heated evenly to 770 °C in 25 min, held for 20 min, and then naturally cooled to room temperature. Finally, the MoS₂ nanotubes are obtained on SiO₂/Si and mica substrates.

Synthesis of MoO₂ nanowires

Like the preparation of MoS₂ nanotubes, MoO₂ nanowires were synthesized as an intermediate material. The sole difference is that the sulfur source has been removed from the quartz tube within the furnace, resulting in the formation of tetragonal-phase MoO₂ nanowires on SiO₂/Si substrates.

Obtaining samples at the initial stage of sulfurization

During the synthesis of MoS₂ nanotubes, the reaction was deliberately interrupted as soon as the temperature of the tube furnace reached 770 °C, followed by rapid cooling to room temperature. The resulting sample, representing the initial stage of sulfurization, consists of a MoO₂–MoS₂ composite. This intermediate product enables the investigation of the sulfurization transformation pathway of the material.

Characterizations

Optical images were acquired with a ZEISS Primotech microscope. X-ray photoelectron spectroscopy (XPS, Kratos AXIS Ultra DLD) is carried out using an Al K_α ($h\nu=1486.6$ eV) source with an operating power of 150 W, and the analysis area is 700 μm × 300 μm. SEM images were obtained by a Field Emission Scanning Electron Microscope (FESEM, Gemini SEM 300). Raman and PL spectra were carried out using an excitation laser of 532 nm from a WITEC alpha 300R Raman system. Resonance Raman measurements in which the excitation wavelength is tuned to match an electronic transition of MoS₂, thereby significantly enhancing defect-sensitive vibrational modes, were performed using a Raman spectroscopic system (Renishaw, InVia) equipped with a 633 nm wavelength excitation laser. AFM topography measurements were conducted using an Asylum Research Cypher S system. The PMMA-assisted wet-transfer method was used to prepare STEM samples, and the cross-section samples were prepared using Zeiss Crossbeam 540 focused ion beam (FIB) with a gallium ion source. TEM was performed using FEI Themis Z transmission electron microscope operated at 300 kV. Atomic-resolution HAADF-STEM images were conducted on an aberration-corrected JEOL ARM-200CF (S)TEM equipped with a cold field-emission gun, operating at 200 kV, and an Advanced STEM Corrector (ASCOR) probe corrector. The beam convergence semi-angle is 28 mrad, and the HAADF collection angle is 65–280 mrad. The EDX spectra were collected using an Oxford X-Max TLE 100 mm² windowless SDD detector. The SHG characteristics of the MoS₂ nanotubes were evaluated using a home-built vertical microscope setup with the reflection geometry. A fiber pulse laser with a central wavelength of 1558 nm (PriTel Inc., with a pulse width of 8.8 ps and repetition rate of 18.8 MHz) was used as the fundamental pump source. The pulse laser was focused using the 50× objective (with a numerical aperture of 0.75), and the focused laser spot is about 2 μm. The SHG signal scattered from the MoS₂ nanotubes was collected using the same objective lens and examined using a spectrometer (Princeton Instruments, SP2558 and 100BRX) equipped with a cooled silicon CCD camera. To investigate the polarization dependence of the SH radiation, a circularly polarized pump laser was passed through a rotating polarizer to achieve linear polarizations along different directions. Another polarizer was then placed in the signal collection path and rotated to match the pump polarization to gather the parallel components of the SHG signal.

Device fabrication and measurement

The SiO₂/Si substrate bearing the as-grown MoS₂ nanotubes was first spin-coated with LOR 5A (Nippon Kayaku, USA), followed by S1805 (Merck, Germany). Micro-Writer (ML3 Serial) was then used to define the electrode patterns. After developing the patterns in the developer (Micro-posit MF-319), electron-beam evaporation and the lift-off process were adopted to deposit the metal contacts. The electrical measurements were carried out in a probe station connected to a

semiconductor parameter analyzer (PDA FS380 Pro, Platform Design Automation).

Simulation methods

Computational details for Raman-mode calculations of tetragonal MoO₂ nanowires: The calculations of crystal structure optimization of tetragonal MoO₂ (I4/m) and vibrational mode analysis were performed using the VASP⁴³ software package with the PBE functional⁴⁴ and an energy cutoff of 400 eV. The lattice parameters were $a=10.623$ Å, $b=10.623$ Å, $c=3.264$ Å. A Γ -centered k-point mesh of $1\times1\times4$ was employed. The vibrational eigenvectors were projected onto the atomic coordinates and visualized with VESTA⁴⁵.

Computational details for electronic structure and curvature-induced polarization of MoS₂ nanotubes: First-principles DFT calculations were performed using the Vienna Ab initio Simulation Package (VASP)⁴³. The exchange-correlation energy was treated within the Perdew–Burke–Ernzerhof (PBE) generalized gradient approximation⁴⁴. The plane-wave basis set with a kinetic energy cutoff of 500 eV was employed. For the geometry optimization and static self-consistent calculations, the Γ -center scheme was sampled with a $12\times1\times1$ grid within the Brillouin zone. The structure relaxation considering the atomic positions was performed by the conjugate gradient (CG) scheme until the maximum force on each atom was less than 10^{-3} eV Å⁻¹, and the total energy was converged to 10^{-6} eV using the Gaussian smearing method.

Photovoltaic response measurements

Electrical measurements, including I – V characterizations and photocurrent responses, were performed using a semiconductor device analyzer (PDA FS380 Pro, Platform Design Automation) under vacuum conditions. MoS₂ nanotubes were illuminated by an excitation laser (wavelength of 635 nm) with a spot size of ≈ 2.5 μm. The line-scan mapping of photocurrent was carried out using a laser of 532 nm by the 100× objective lens from a WITEC alpha 300R Raman system under ambient conditions. The laser spot size was ≈ 1 μm.

Reporting summary

Further information on research design is available in the Nature Portfolio Reporting Summary linked to this article.

Data availability

The data that support the findings of this study are available from the corresponding authors upon request. Source data are provided with this paper.

References

- Xue, G. et al. WS₂ ribbon arrays with defined chirality and coherent polarity. *Science* **384**, 1100–1104 (2024).
- Tenne, A. R., Margulis, L., Genut, M. & Hodes, G. Polyhedral and cylindrical structures of tungsten disulphide. *Nature* **360**, 444–446 (1992).
- Xiang, R. et al. One-dimensional van der Waals heterostructures. *Science* **367**, 537–542 (2020).
- Zhao, B. et al. High-order superlattices by rolling up van der Waals heterostructures. *Nature* **591**, 385–390 (2021).
- Nakanishi, Y. et al. Structural diversity of single-walled transition metal dichalcogenide nanotubes grown via template reaction. *Adv. Mater.* **35**, 2306631 (2023).
- Sreedhara, M. B. et al. Nanotubes from lanthanide-based misfit-layered compounds: understanding the growth, thermodynamic, and kinetic stability limits. *Chem. Mater.* **36**, 4736–4749 (2024).
- Guo, J. et al. Preparation of single-crystal MoS₂ nanotubes and 1D van der Waals heterostructures. *Adv. Funct. Mater.* **35**, 2408703 (2025).

8. Remškar, M. Inorganic nanotubes. *Adv. Mater.* **16**, 1497–1504 (2004).
9. Sun, Y. et al. Mesoscopic sliding ferroelectricity enabled photo-voltaic random access memory for material-level artificial vision system. *Nat. Commun.* **13**, 5391 (2022).
10. Qin, F. et al. Superconductivity in a chiral nanotube. *Nat. Commun.* **8**, 14465 (2017).
11. Zhang, Y. et al. Enhanced intrinsic photovoltaic effect in tungsten disulfide nanotubes. *Nature* **570**, 349–353 (2019).
12. Cardoso, G. L., Piquini, P. C. & Ahuja, R. From monolayers to nanotubes: toward catalytic transition-metal dichalcogenides for hydrogen evolution reaction. *Energy Fuels* **35**, 6282–6288 (2021).
13. Bar-Saden, M. & Tenne, R. The gold ticket to achiral WS₂ nanotubes. *Nat. Mater.* **23**, 310–311 (2024).
14. Weng, M. et al. Catalytic chemical vapor deposition and structural analysis of MoS₂ nanotubes. *Jpn J. Appl. Phys.* **57**, 030304 (2018).
15. An, Q. et al. Direct growth of single-chiral-angle tungsten disulfide nanotubes using gold nanoparticle catalysts. *Nat. Mater.* **23**, 347–355 (2024).
16. Fan, H. J., Gosele, U. & Zacharias, M. Formation of nanotubes and hollow nanoparticles based on Kirkendall and diffusion processes: a review. *Small* **3**, 1660–1671 (2007).
17. Liu, Z. et al. 2D nanotubes, 2D nanomeshes, and 2D in-plane films through one single chemical vapor deposition route. *ACS Nano* **13**, 3896–3909 (2019).
18. Chithaiah, P. et al. Solving the “MoS₂ nanotubes” synthetic enigma and elucidating the route for their catalyst-free and scalable production. *ACS Nano* **14**, 3004–3016 (2020).
19. Kundrát, V. et al. Mechanism of WS₂ nanotube formation revealed by in situ/ex situ imaging. *ACS Nano* **18**, 12284–12294 (2024).
20. Kundrát, V. et al. Submillimeter-long WS₂ nanotubes: the pathway to inorganic buckypaper. *Nano Lett.* **23**, 10259–10266 (2023).
21. Yang, S. Y. et al. Above-bandgap voltages from ferroelectric photovoltaic devices. *Nat. Nanotechnol.* **5**, 143–147 (2010).
22. Spanier, J. E. et al. Power conversion efficiency exceeding the Shockley–Queisser limit in a ferroelectric insulator. *Nat. Photonics* **10**, 611–616 (2016).
23. Gong, Y. et al. Tellurium-assisted low-temperature synthesis of MoS₂ and WS₂ monolayers. *ACS Nano* **9**, 11658–11666 (2015).
24. Liu, H. et al. Tellurium-assisted and space-confined growth of graphene single crystals. *Carbon* **173**, 54–60 (2021).
25. Li, S. et al. Vapour–liquid–solid growth of monolayer MoS₂ nanoribbons. *Nat. Mater.* **17**, 535–542 (2018).
26. Luo, L. et al. Ultra-low power consumption flexible sensing electronics by dendritic bilayer MoS₂. *InfoMat* **6**, e12605 (2024).
27. Park, J. C. et al. Phase-engineered synthesis of centimeter-scale 1T' and 2H-molybdenum ditelluride thin films. *ACS Nano* **9**, 6548–6554 (2015).
28. Tummala, P. P. et al. Large area growth and phase selectivity of MoTe₂ nanosheets through simulation-guided CVD tellurization. *Adv. Mater. Interfaces* **10**, 2200971 (2023).
29. Gong, Y. et al. Vertical and in-plane heterostructures from WS₂/MoS₂ monolayers. *Nat. Mater.* **13**, 1135–1142 (2014).
30. Zhou, J. et al. A library of atomically thin metal chalcogenides. *Nature* **556**, 355–359 (2018).
31. Rothman, A. et al. Real-time study of surface-guided nanowire growth by in situ scanning electron microscopy. *ACS Nano* **16**, 18757–18766 (2022).
32. Sutter, P., Wimer, S. & Sutter, E. Chiral twisted van der Waals nanowires. *Nature* **570**, 354–357 (2019).
33. Sutter, E., French, J. S., Komsa, H.-P. & Sutter, P. 1D germanium sulfide van der Waals bicrystals by vapor–liquid–solid growth. *ACS Nano* **16**, 3735–3743 (2022).
34. An, Q. et al. Direct growth of single-chiral-angle tungsten disulfide nanotubes using gold nanoparticle catalysts. *Nat. Mater.* **23**, 347–355 (2023).
35. Remškar, M., Škraba, Z., Ballif, C., Sanjinés, R. & Lévy, F. Stabilization of the rhombohedral polytype in MoS₂ and WS₂ microtubes: TEM and AFM study. *Surf. Sci.* **433–435**, 637–641 (1999).
36. Seifert, G., Terrones, H., Terrones, M., Jungnickel, G. & Frauenheim, T. Structure and electronic properties of MoS₂ nanotubes. *Phys. Rev. Lett.* **85**, 146–149 (2000).
37. Frey, G. L., Elani, S., Homyonfer, M., Feldman, Y. & Tenne, R. Optical-absorption spectra of inorganic fullerene-like MS₂ (M = Mo, W). *Phys. Rev. B* **57**, 6666–6671 (1998).
38. Piskunov, S. et al. First-principles evaluation of the morphology of WS₂ nanotubes for application as visible-light-driven water-splitting photocatalysts. *ACS Omega* **4**, 1434–1442 (2019).
39. Wang, Z. et al. Self-scrolling MoS₂ metallic wires. *Nanoscale* **10**, 18178–18185 (2018).
40. Jiang, H. et al. Inversion symmetry broken in 2H phase vanadium-doped molybdenum disulfide. *Nanoscale* **13**, 18103–18111 (2021).
41. Qian, Q. et al. Chirality-dependent second harmonic generation of MoS₂ nanoscroll with enhanced efficiency. *ACS Nano* **14**, 13333–13342 (2020).
42. Kim, B., Park, N. & Kim, J. Giant bulk photovoltaic effect driven by the wall-to-wall charge shift in WS₂ nanotubes. *Nat. Commun.* **13**, 3237 (2022).
43. Kresse, G. & Furthmüller, J. Efficient iterative schemes for ab initio total-energy calculations using a plane-wave basis set. *Phys. Rev. B* **54**, 11169–11186 (1996).
44. Perdew, J. P., Burke, K. & Ernzerhof, M. Generalized gradient approximation made simple. *Phys. Rev. Lett.* **77**, 3865–3868 (1996).
45. Momma, K. & Izumi, F. VESTA 3 for three-dimensional visualization of crystal, volumetric and morphology data. *J. Appl. Crystallogr.* **44**, 1272–1276 (2011).

Acknowledgements

The authors gratefully acknowledge financial support from the National Natural Science Foundation of China (62288102, 62371397, 62304182, and 62471396), the Fundamental Research Funds for the Central Universities, and the Open Test Funding Project from the Analytical & Testing Center of Northwestern Polytechnical University (2023T008). Y.W. acknowledges the Facility for analysis, characterization, testing, and simulation (FACTS), Nanyang Technological University, Singapore, for the use of their electron microscopy facilities. Z.L. acknowledges the support from the National Research Foundation, Singapore, under its Competitive Research Programme (CRP) (NRF-CRP22-2019-0007). This research is supported by A*STAR under its AME IRG Grant (Project No. A2083c0052), supported from the Singapore Ministry of Education under its Academic Research Fund Tier 2 (T2EP50223-0008) and Tier 3 Programme “Geometrical Quantum Materials” (MOE2018-T3-1-002), and its Research Centre of Excellence award to the Institute for Functional Intelligent Materials (Project No. EDUNC-33-18-279-V12).

Author contributions

L. Luo conceived the concept, designed the experiments, and completed the manuscript. Y. Wu performed STEM characterizations. L. Li and Z. Zhang carried out the DFT calculation. L. Luo prepared and characterized the samples. L. Luo, L. Zheng, M. Xu, W. Li, Y. He, Q. Fu, and J. Yang analyze the characterization results. L. Luo constructed and tested the BPVE and electrical properties of the sample with the help of C. Zhu, G. Wu, and Q. Wu. R. Duan prepared the 3R-MoS₂ flake. X. Wang and Z. Liu revised the paper. All authors discussed the results and commented on the manuscript. W. Huang, X. Wang, and Z. Liu conceived and supervised the project.

Competing interests

The authors declare no competing interests.

Additional information

Supplementary information The online version contains supplementary material available at <https://doi.org/10.1038/s41467-025-63333-1>.

Correspondence and requests for materials should be addressed to Xuewen Wang or Zheng Liu.

Peer review information *Nature Communications* thanks Vojtech Kundrat, Rahul Rao, and the other anonymous reviewer(s) for their contribution to the peer review of this work. A peer review file is available.

Reprints and permissions information is available at <http://www.nature.com/reprints>

Publisher's note Springer Nature remains neutral with regard to jurisdictional claims in published maps and institutional affiliations.

Open Access This article is licensed under a Creative Commons Attribution-NonCommercial-NoDerivatives 4.0 International License, which permits any non-commercial use, sharing, distribution and reproduction in any medium or format, as long as you give appropriate credit to the original author(s) and the source, provide a link to the Creative Commons licence, and indicate if you modified the licensed material. You do not have permission under this licence to share adapted material derived from this article or parts of it. The images or other third party material in this article are included in the article's Creative Commons licence, unless indicated otherwise in a credit line to the material. If material is not included in the article's Creative Commons licence and your intended use is not permitted by statutory regulation or exceeds the permitted use, you will need to obtain permission directly from the copyright holder. To view a copy of this licence, visit <http://creativecommons.org/licenses/by-nc-nd/4.0/>.

© The Author(s) 2025